ACS APPLIED NANO MATERIALS

www.acsanm.org Article

Inhibition of Silica Nanoparticle Adhesion to Poly(vinyl alcohol) Surfaces by Ammonia-Mediated Hydration: Implications for Effective Post-Chemical–Mechanical Planarization Cleaning

Takahiko Ikarashi, Takumi Yoshino, Naoki Nakajima, Kazuki Miyata, Keisuke Miyazawa, Ygor Morais Jaques,* Adam S. Foster, Megumi Uno, Chikako Takatoh, and Takeshi Fukuma*

Cite This: *ACS Appl. Nano Mater.* 2021, 4, 71–83

Read Online

ACCESS | Metrics & More | Article Recommendations | Supporting Information

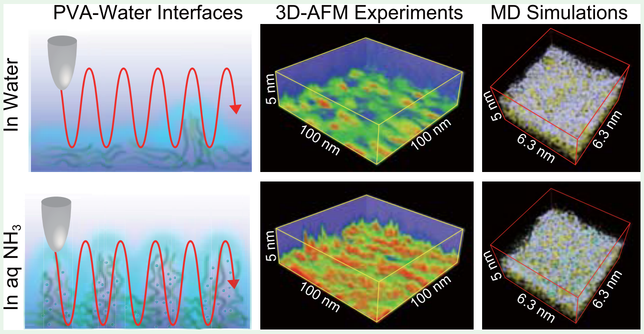

ABSTRACT: Adhesion of silica abrasive nanoparticles to a poly(vinyl alcohol) (PVA) brush surface in post-CMP (chemical–mechanical planarization) cleaning leads to serious problems in yield enhancement of semiconductor fabrication. However, the nanoscale adhesion mechanism and its correlation with process conditions have hardly been understood. In this study, we investigated the influence of ammonia in the cleaning solution on silica nanoparticle adhesion to a PVA surface. By atomic force microscopy (AFM), we directly measured adhesion forces between a nanoscale silica probe and a PVA brush surface in various solutions and found that ammonia has a significant inhibitory effect against silica nanoparticle adhesion to a PVA surface. Importantly, we found that this effect cannot be explained by the electrostatic interactions alone but also involves steric repulsion between silica and hydrated PVA. We also performed molecular-scale three-dimensional scanning force microscopy (3D-SFM) imaging and contact angle measurements and found that ammonia promotes hydration and swelling of PVA. Furthermore, we performed molecular dynamics simulations and found that ammonia promotes dynamic rearrangements of hydrogen-bonding networks (HBNs) at a PVA–water interface, giving extra flexibility to the PVA chains. Such flexibility promotes local swelling of PVA and inhibits silica nanoparticle adhesion to a PVA surface. This provides important guidelines for optimizing nanoscale structures and interactions of brush surfaces and abrasive nanoparticles in post-CMP cleaning.

KEYWORDS: *three-dimensional atomic force microscopy, poly(vinyl alcohol), silica nanoparticles, ammonia water, post-CMP cleaning*

■ INTRODUCTION

Rapid development of advanced information technologies demands continuous miniaturization of semiconductor devices. To this end, tremendous efforts have been made to overcome major technological challenges, including fabrication of high aspect ratio nanostructures, introduction of EUV lithography, an increase of channel mobility, and development of high-*k* dielectric materials. While these efforts enabled the reduction of device sizes to the nanometer scale, fabrication and operation are becoming increasingly sensitive to nanoscale defects. Therefore, the development of nanolevel cleaning technologies has become one of the key challenges for yield enhancement of semiconductor fabrication.

This issue is particularly serious for cleaning after a chemical–mechanical planarization (CMP) process (i.e., post-CMP cleaning). At present, most of the semiconductor fabrication processes require more than several CMP steps, where a wafer surface is polished in a slurry containing abrasive nanoparticles and various organic compounds. This process leaves significant amounts of abrasive nanoparticles, organic materials, and wear debris on a wafer surface.[1] Complete elimination of such a large amount of nanoscale contaminants from a 12-in. wafer is a great challenge, even with the latest cleaning technology.

Among various methods used for post-CMP cleaning, the brush scrubbing method has been accepted as the most efficient way to remove contaminants.[2,3] In this method, a rotating poly(vinyl alcohol) (PVA) brush (Figure 1a) is pressed onto a laterally rotating wafer in an aqueous environment. To improve the efficiency of scrubbing, various process conditions and methods have been explored.[4−12] In addition, nanoparticle removal mechanisms have been studied from theoretical and experimental aspects.[13−17] However,

Received: August 26, 2020
Accepted: December 4, 2020
Published: December 16, 2020

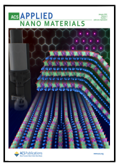

https://dx.doi.org/10.1021/acsanm.0c02308

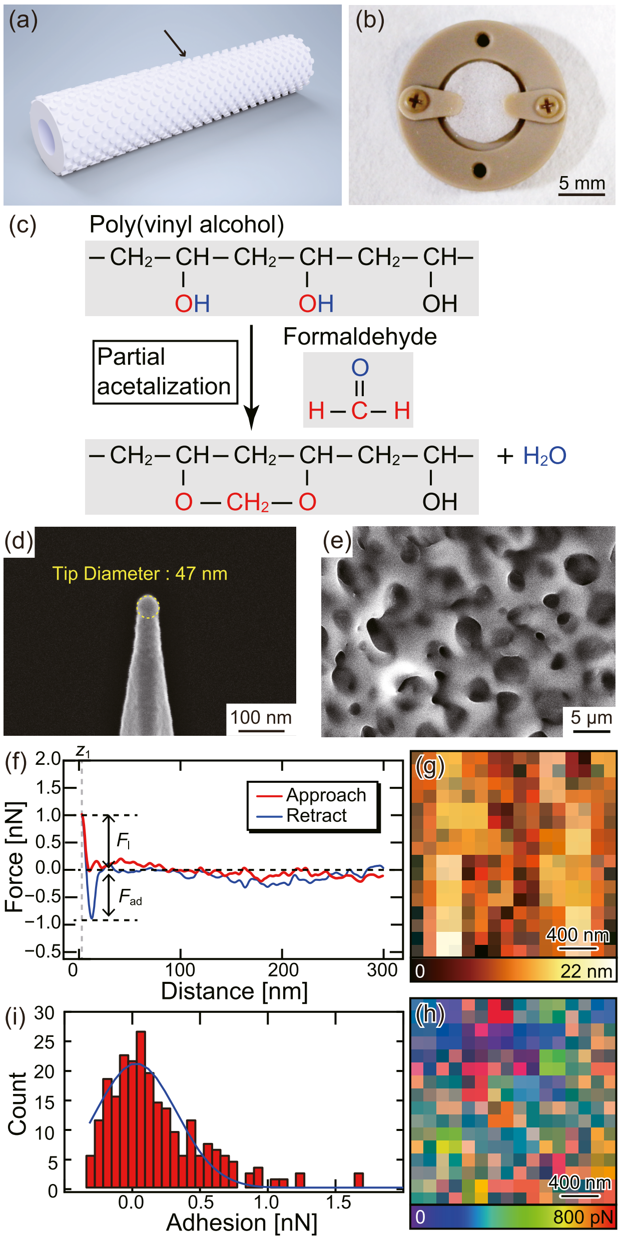

Figure 1. Samples and methods used for the atomic force microscopy (AFM) adhesion force mapping. (a) Illustration of the PVA brush for post-CMP cleaning of a Si wafer. (b) 1 mm thick PVA film attached to the AFM sample holder. This film was sliced from the topmost part of a nodule at the PVA brush surface. (c) Chemical structure and fabrication process of the PVA brush. (d) Scanning electron microscopy (SEM) image of the AFM tip apex, which was coated with a Si film to increase the diameter to 50 nm: a typical size of the silica beads for a CMP process. (e) SEM image of the PVA sample surface. (f) Typical approach and retraction force curves measured on a PVA sample. (g, h) Example of the two-dimensional (2D) height and F_{ad} images derived from a three-dimensional (3D) force map. (i) Histogram of F_{ad} derived from (h).

these previous efforts mostly focused on nanoparticle−wafer interactions so that phenomena and mechanisms related to nanoparticle−PVA interactions have not been well understood, especially on the nanometer scale.

Recently, such interactions between nanoparticles and PVA have attracted special attention due to growing demands for reducing cross-contamination between wafers.[3,18−20] During post-CMP cleaning, some nanoparticles removed from a wafer are adsorbed on the PVA brush and redeposited on the wafer, leading to a low removal efficiency and/or cross-contamination between different wafers. In addition, these nanoparticles can cause serious damage to the wafer and PVA brush during cleaning. To solve these issues, optimal process parameters and brush cleaning methods have been investigated.[3,18−21] However, a detailed understanding of a nanoparticle−PVA interaction has remained elusive. In particular, the influence of hydration on nanoparticle adhesion to a PVA brush has hardly been investigated. This is a serious problem, as hydration is known to play a critical role in the antifouling mechanism of polymer surfaces in an aqueous environment.[22,23] In addition, PVA has an excellent water absorption capability[24−26] and hence its hydration and swelling could have a great impact on the nanoparticle−PVA interaction. Owing to the wide applicability of PVA in an aqueous environment, the hydration of PVA has been intensively investigated by molecular dynamics (MD) simulation,[24,26,27] NMR measurements,[25,28,29] and differential scanning calorimetry (DSC).[28,30] However, its influence on nanoparticle adhesion has not been investigated.

Regarding nanoparticle−PVA interactions, a previous study reported on ζ-potential measurements of PVA and silica nanoparticle surfaces with various pH conditions.[20] This study found that both surfaces are negatively charged in a high pH condition and suggested that their repulsive interaction may help in removing nanoparticles from a PVA surface in dilute ammonia water, which is one of the most commonly used solutions for post-CMP cleaning. However, the adhesion behavior depends not only on the electrostatic interaction but also on the hydration and flexibility of the polymer chains.[22,23] In particular, ammonia is known to enhance the hydration of the atmospheric ions such as HSO_4^- and methanesulfonate to form an aerosol.[31,32] Thus, the influence of ammonia on the PVA hydration and its impact on the water-mediated particle−PVA interaction should be taken into account.

One reason for the absence of such studies lies in the difficulties inherent in the direct measurement of interactions between a nanoparticle and a corrugated PVA brush surface in a liquid environment. In the previous studies, scanning electron microscopy (SEM) has been commonly used for imaging nanoparticles adsorbed on a PVA surface.[11,19,20,33] In addition, fluorescence microscopy has been employed for real-time observations of dynamic nanoparticle movements during the PVA brush scrubbing.[33,34] However, these methods do not allow us to directly measure the interaction forces acting between the nanoparticles and the PVA surfaces. Furthermore, PVA is known as a water-soluble polymer and, hence, the interface could present complicated three-dimensional (3D) mixtures of flexible polymer chains, water, and ammonia. Direct observation of such nanoscale 3D structures at a solid−liquid interface has been difficult for the conventional measurement technologies.

To overcome this difficulty, here, we use two atomic force microscopy (AFM) techniques with a 3D tip scan. One of them is a relatively common technique, while the other is highly advanced. AFM[35] is a powerful tool for imaging surface structures with the nanoscale resolution even in liquid.[36] In addition, it has been widely used for direct measurements of adhesion forces between an AFM tip and a flat surface.[36] By modifying the tip apex to mimic the structure and/or surface properties of a target nanoparticle and taking force curves at *xy*-arrayed positions of the surface, the nanoscale distribution of the adhesion force acting between the nanoparticle and the surface can be measured with pico-Newton force sensitivity. This technique is known as the force mapping method and has become a relatively common technique.[37−39] However, special care must be taken for the present study as the size of the abrasive nanoparticles is less than 50 nm and the PVA brush is not a flat sample.

Another AFM technique that we used is 3D scanning force microscopy (3D-SFM) combined with the frequency modulation (FM) detection method.[40] In this technique, a tip is scanned in a 3D interfacial space and the force applied to the tip is recorded to produce a 3D force map. During the scan, the tip interacts with surrounding water and surface structures so that the obtained force map represents the spatial distribution of these interacting molecules. So far, this technique has been used for visualizing subnanometer-scale 3D hydration structures formed on various minerals and biomolecules.[41] In addition, it was also used for visualizing the 3D hydration structures formed on silica beads functionalized with organic molecules,[23] and the results were successfully discussed in relation to the antifouling capability of the surface modification. However, 3D-SFM imaging of polymer−water interfaces has not been reported yet. In contrast to the interfaces previously observed by this technique, a polymer−water interface is expected to show a much more complicated mixture of polymer chains and water. Therefore, methods for measurement and data analysis have not been established yet.

In this study, we have investigated the nanoscale hydration behavior of a PVA surface and its influence on the silica nanoparticle adhesion to a PVA brush surface for efficient application of these materials to post-CMP cleaning. In particular, special attention has been paid to the contribution of ammonia, which generally exists in a post-CMP cleaning solution. We perform AFM adhesion force mapping with a silica probe having a 50 nm apex diameter on a sample sliced from a PVA brush for post-CMP cleaning. In addition, 3D-SFM measurements are performed on a PVA thin film formed on a highly oriented pyrolytic graphite (HOPG) surface. For the analysis of the obtained 3D data, we have developed a method for deriving information on the nanoscale distribution of the polymer hydration state. To understand the role of ammonia, we perform these AFM experiments in various solutions, including water and aqueous solutions of NH_3, KOH, and NH_4Cl. Furthermore, we perform MD simulations of PVA−water and PVA−ammonia water interfaces to understand the mechanism of the ammonia-mediated hydration of a PVA surface.

■ RESULTS AND DISCUSSION

Adhesion Force Measurements. First, we have established a method for adhesion force mapping directly on a PVA brush surface with a silica probe having a diameter close to the typical size of an abrasive particle, as shown in Figure 1. A PVA brush used for post-CMP cleaning (Figure 1a) has a cylindrical shape with many nodules on its surface. During cleaning, the nodule surface is pressed onto a wafer surface to remove the abrasive particles. This surface is typically hardened by heat treatment to give enough mechanical strength. In addition, the PVA brush used for the post-CMP cleaning is typically hardened by the partial acetalization, as shown in Figure 1c. Thus, it is desirable to measure adhesion forces directly on the nodule surface. For this purpose, we sliced the top part of a nodule with a thickness of 1 mm and mounted it on the sample holder, as shown in Figure 1b.

AFM adhesion force measurements between a particle and a flat surface are often performed with a colloidal probe that is fabricated by attaching a micrometer-scale spherical bead to a tip apex. However, this method is applicable only for a micrometer-scale bead and nanoscale particles are too small to be manipulated by a micromanipulator. Although we can use a nanomanipulator integrated into an SEM, this typically results in the deposition of carbon contaminants onto the particle surface. In this study, we coated an AFM tip with a silicon film to obtain a diameter of around 50 nm (Figure 1d). After immersion into water, the surface is fully oxidized so that the tip apex can mimic the structure and surface properties of a silica abrasive particle. We confirmed that the tip apex structure remains almost the same even after repeated adhesion force measurements by transmission electron microscopy (TEM) observations (Fig. S1).

The surface of a nodule is not perfectly flat but has micrometer-scale corrugations, as shown in Figure 1e. Such corrugations of the sliced PVA sample are visible even with an optical microscope. Thus, with an optical view, we aligned an AFM tip to a relatively flat region. After the tip approach, we performed a force mapping at 16 × 16 *xy*-arrayed positions over an area of 2×2 μm^2. Figure 1f shows a typical approach and retraction force curves. These curves are shown after a linear subtraction of the long-range component and smoothing (see Figure S2 in the Supporting Information for more details).

During the tip approach, a repulsive force starts to increase from a certain z tip position. When the repulsive force reaches a predetermined threshold value referred to as a loading force (F_l), the tip approach is stopped. At this position (z_0), the tip remains for a predefined period referred to as the dwell time (t_d). After the dwelling, tip retraction is started. This leads to a decrease of the force, followed by a sudden detachment of the tip from the surface. We define this maximum attractive force just before the detachment as an adhesion force (F_{ad}).

By applying a similar analysis for all of the force curves, a two-dimensional (2D) distribution map of the height (z_0) and adhesion force (F_{ad}) are obtained as shown in Figure 1g,h, respectively. By comparing these two images, we found no significant correlation between them (see Figure S2f for more details). The obtained F_{ad} map is plotted as a histogram and fitted to a Gauss function to obtain a representative F_{ad} value for each of the measurement conditions. In this way, we measured adhesion forces with various t_d (0−10 s), F_l (0.5−50 nN), and solution conditions (pure water and aqueous solutions of NH_3, KOH, and NH_4Cl). To understand the influence of ammonia, we compared the results obtained in pure water and 0.5 wt % aq NH_3. This concentration is typical for ammonia water used for post-CMP cleaning. In some of the experiments, we also used aq KOH and aq NH_4Cl with OH^- and NH_4^+ concentrations equal to those in the 0.5 wt % aq NH_3, respectively. This is for understanding the contributions of these individual ionic components in ammonia water.

With the force mapping method, we have investigated the t_d and F_l dependence of F_{ad} with various solution conditions at room temperature (∼25 °C), as shown in Figure 2. Figure 2a shows the t_d dependence measured with a F_l of 1.5 nN. In pure water, F_{ad} increases with increasing t_d. This t_d dependence becomes slightly weaker when t_d exceeds 2 s. In contrast, in aq NH_3, almost no adhesion force was detected regardless of t_d. Such a difference is also confirmed in the F_l dependence curve

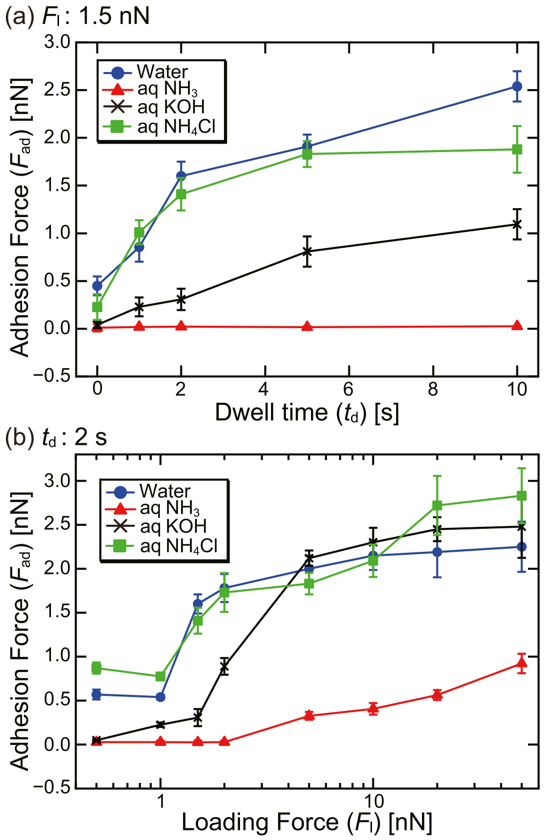

Figure 2. Dependence of F_{ad} on t_d and F_l measured with various solution conditions, including pure water and aqueous solutions of NH_3, KOH, and NH_4Cl. (a) F_l dependence. (b) t_d dependence.

shown in Figure 2b. In pure water, F_{ad} shows a sharp increase when F_l exceeds 1 nN and quickly reaches a saturated value of around 2 nN. In aq NH_3, F_{ad} shows a much slower increase when F_l exceeds 2 nN. These results show that ammonia water has an inhibitory effect on the silica adhesion to a PVA brush surface.

The 0.5 wt % aq NH_3 contains 294 mM NH_3, 2.3 mM NH_4^+, and 2.3 mM OH^- (pH ≈ 11.4). To understand the contributions from these individual components, we also performed measurements in aq KOH (pH: 11.4) and 2.3 mM aq NH_4Cl, as shown in Figure 2. Note that OH^- in aq KOH or NH_4^+ in NH_4Cl solution may behave differently from that in aq NH_3. However, using different solutions with the same OH^- or NH_4^+ concentration, we checked if the observed adhesion resistance can be explained only by the individual ionic components.

For aq NH_4Cl, both the t_d and F_l dependence show almost the same behaviors as observed in pure water. This suggests that the contribution from NH_4^+ is negligible. Note that Cl^- in aq NH_4Cl could potentially influence the behavior of NH_4^+. However, as NH_4Cl is perfectly ionized in an aqueous solution, their interplay is expected to be relatively small.

For aq KOH, F_{ad} shows an intermediate behavior between those observed in pure water and aq NH_3, especially at a F_l lower than 2 nN. For example, with a F_l of 1.5 nN, F_{ad} increases with increasing t_d, but the dependence is weaker than that in pure water (Figure 2a). Once F_l exceeds 2 nN, the F_{ad} rapidly increases to reach a saturated value (~2 nN) similar to that observed in pure water (Figure 2b). These results show that OH^- ions (i.e., high pH conditions) have an inhibitory effect on the silica adhesion to a PVA brush surface at a low F_l range. However, the inhibitory effect observed in aq NH_3 is much more significant than that in aq KOH, especially at a high F_l range. Therefore, NH_3 molecules could play a critical role in the observed inhibitory effect.

ζ-Potential Measurements. The antifouling mechanism of a polymer surface is often discussed in relation to electrostatic interactions, hydration forces, and steric repulsion. Among them, to understand the contribution from the electrostatic interactions,[42−45] we measured the ζ-potential of silica and PVA surfaces with various pH values, as shown in Figure 3. For the PVA measurements, we used a sample prepared in the same way as the one used for the AFM experiments (Figure 1b). For the silica measurements, we used particles with a diameter of ~50 nm. Figure 3 shows that the ζ-potential of the PVA surface decreases with the increasing pH, while that of the silica surface shows little pH dependence. This behavior does not depend on the solution (i.e., NH_3 or KOH solution) used for adjusting the pH. Thus, similar electrostatic interactions are expected in these solutions.

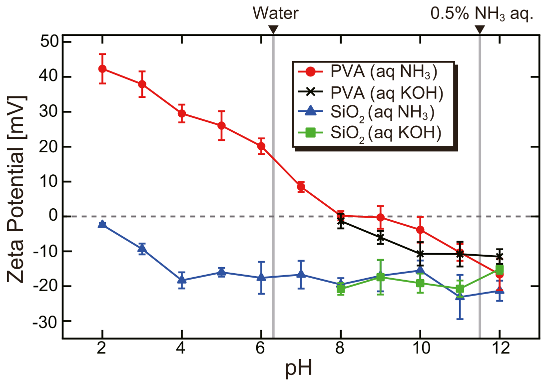

Figure 3. pH dependence of the ζ-potential measured with and without 0.5 wt % NH_3. The pH was adjusted by adding HCl solution in the low pH regime, while NH_3 or KOH solution was added in the high pH regime.

In a neutral solution such as Milli-Q water and aq NH_4Cl, silica and PVA surfaces have opposite charges so that an attractive force between them could enhance the silica adhesion to a PVA surface. In contrast, in an alkaline solution such as aq NH_3 and aq KOH, both surfaces are negatively charged so that a repulsive force between them could inhibit such an adhesion. Such electrostatic interactions can explain the relatively low F_{ad} observed in high pH solutions (Figure 2). These results and arguments are largely consistent with the previous studies on the silica−PVA interactions by ζ-potential measurements.[20]

However, this mechanism does not explain the significant difference between the NH_3 and KOH solutions. In addition, the strong t_d dependence of F_{ad} in the time scale of several seconds cannot be explained only by the electrostatic interactions. In contrast, the other mechanisms such as hydration or steric repulsion could involve relatively slow processes such as dehydration or conformational changes of polymer chains. Therefore, it is likely that the NH_3 molecules have a significant influence on the hydration of a PVA surface. The role of hydrogen bonding at the PVA−water interface is discussed in more detail with the simulation results later.

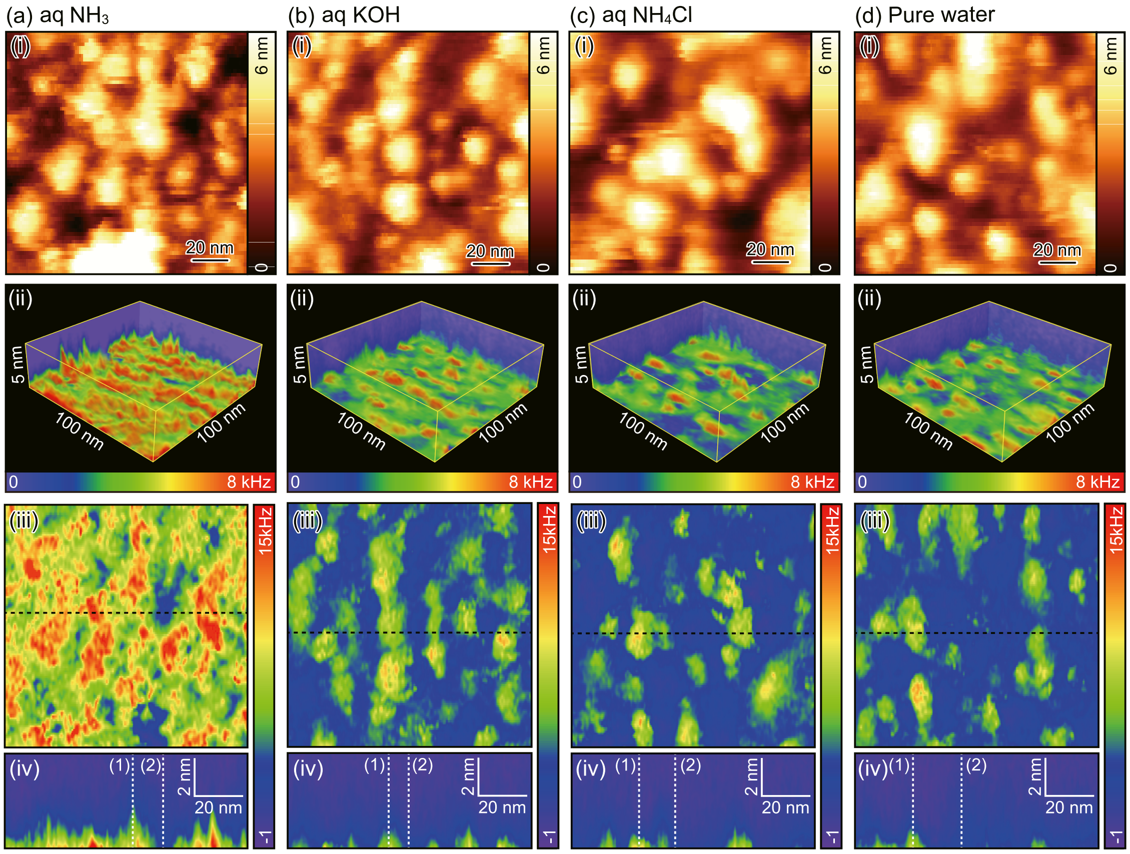

Figure 4. 3D-SFM measurements of PVA−water interfaces in various solutions (Δf_{sp} = 781.2 Hz): (a) aq NH_3 (k = 81.2 N/m, f_0 = 1.36 MHz, Q = 8.3, A = 0.24 nm), (b) aq KOH (k = 77.6 N/m, f_0 = 1.33 MHz, Q = 9.1, A = 0.32 nm), (c) aq NH_4Cl (k = 47.3 N/m, f_0 = 0.887 MHz, Q = 7.5, A = 0.33 nm), and (d) pure water (k = 68.2 N/m, f_0 = 1.1 MHz, Q = 7.8, A = 0.31 nm). (i) 2D height images. (ii) 3D Δf images simultaneously obtained with (i). (iii) xy cross-sections of (ii) obtained at the closest tip position to the surface. (iv) xz cross-sections of (ii) obtained at the dotted lines indicated in (iii).

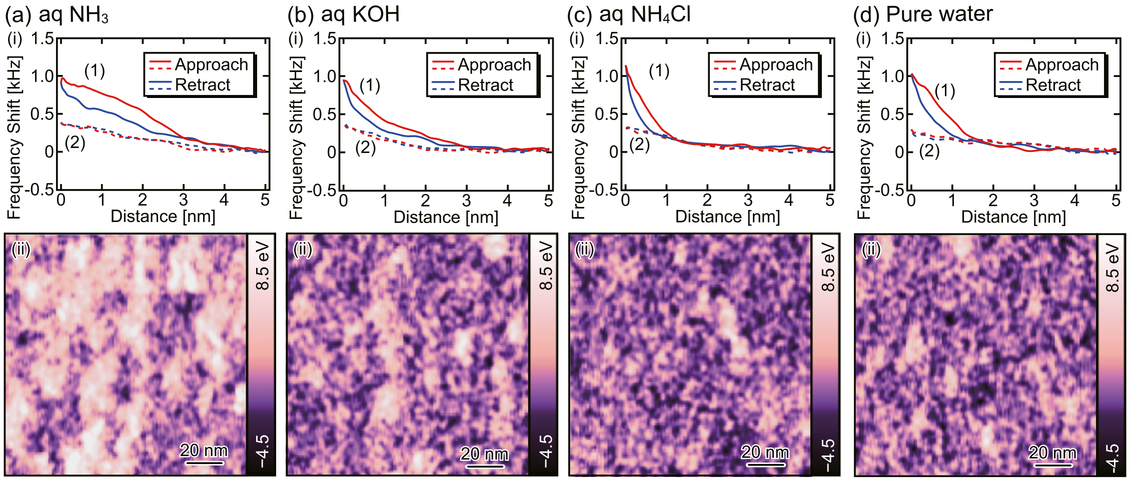

Figure 5. 3D-SFM measurements of PVA−water interfaces in various solutions: (a) aq NH_3, (b) aq KOH, (c) aq NH_4Cl, and (d) pure water. (i) $z\Delta f$ profiles measured at the x positions indicated by the dotted lines in Figure 4(iv). (ii) Lateral distribution of energy dissipation per single z approach and retraction cycle.

3D-SFM Measurements. To understand the influence of NH_3 on the hydration and morphology of a PVA surface, we have performed 3D-SFM measurements at PVA−water interfaces in different solutions, as shown in Figure 4. This experiment was performed with a PVA thin film formed on a highly oriented pyrolytic graphite (HOPG) surface. Although it is ideal to use the PVA brush sample, such a thick and soft sample makes it difficult to achieve a high spatial resolution. In contrast, the PVA thin film is firmly supported by the underlying HOPG substrate and allows for high-resolution imaging. Therefore, we used the PVA thin film as a simplified model to investigate the hydration and swelling behaviors of the poly(vinyl alcohol) chains.

In a 3D-SFM measurement, a 2D height image and a 3D Δf image are simultaneously obtained (see the Methods section for details). In the height images (Figure 4(i)), globular protrusions with a height of a few nanometers are observed in all of the cases. A minor difference may be found between the high pH and low pH conditions. In NH_3 and KOH solutions (i.e., high pH conditions), the protrusions seem to have a more uniform size and a more densely packed distribution than those in aq NH_4Cl and pure water (i.e., low pH conditions).

Such differences are much more clearly confirmed in the 3D Δf images (Figure 4(ii)) and their *xy* and *xz* cross-sections (Figure 4(iii),(iv)). In pure water and aq NH_4Cl, protrusions with a high Δf value (i.e., high repulsive force) are sparsely distributed. The density of these spots is slightly higher in aq KOH and significantly higher in aq NH_3. Comparing this solution dependence with that of F_{ad} (Figure 2), we find a strong correlation: a high density of the high Δf spots seems to provide a low F_{ad}. Thus, these results suggest that the inhibitory effect of the adhesion may originate from these high Δf spots.

To understand the properties of the high Δf spots, *z*-profiles are derived from the *xz* cross-sections (Figure 4(iv)) at the *x* positions (1) inside and (2) outside of the high Δf spots, as shown in Figure 5(i). The *z*-profiles show a clear hysteresis inside the high Δf spots, while no hysteresis was observed outside. The size of the hysteresis loop increases in the order of pure water $\simeq$ aq NH_4Cl < aq KOH < aq NH_3.

To investigate the lateral distribution of the hysteresis, we converted all of the *z*-profiles constituting the 3D Δf images to a force curve and integrated it to obtain energy dissipation (E_d) per single *z* approach and retraction cycle. The obtained energy dissipation maps are shown in Figure 5(ii). As expected, the lateral distribution of the high E_d spots is similar to that of the high Δf spots shown in Figure 4(iii). Thus, the solution dependence of the density of the high E_d spots is also similar to that of the high Δf spots and F_{ad}.

To confirm the consistency between the results obtained with the PVA thin film and the PVA brush sample, we also performed 3D-SFM measurements on the PVA brush samples in aq NH_3 and pure water as shown in Fig. S3. Although the resolution of the images is not as high as that obtained with the thin film, the important features related to the major conclusions are well reproduced. Thus, it is likely that NH_3 has a similar influence on the hydration and swelling behavior of these two polymer samples.

For obtaining molecular-scale insight, we performed a high-resolution 3D-SFM measurement on a high Δf spot in aq NH_3, as shown in Figure 6. The *xy* cross-section (Figure 6a) of the 3D Δf image taken at the *z* position indicated by a red arrow in Figure 6b shows the lateral distribution of the PVA chains as indicated by the white arrows. The AB-z cross-section taken along one of the molecular chains shows a clear line-shaped contrast on the molecular chain. We interpret this line-shaped contrast as a hydration layer rather than a molecular chain. This is because a *z* cross-section taken at this height does not show a line-shaped contrast but a uniform contrast. This cannot be explained by a molecular chain and could be ascribed to a hydration layer. Note that this 3D image visualizes only the top surface of the protruded high Δf spot so that the subsurface polymers are not visualized.

The hysteresis observed in the Δf curves suggests a slow relaxation time of the surface structures deformed during a tip approach. Such behavior can be explained by the removal of water from the swollen polymer. Before immersion into an aqueous environment, the PVA chains are closely packed due to the intermolecular interactions. Upon immersion, some of the polymer chains near the surface could be hydrated and take a more extended conformation with a larger intermolecular distance. Such a local swelling of polymer chains could form a protruded surface structure containing interfacial water.

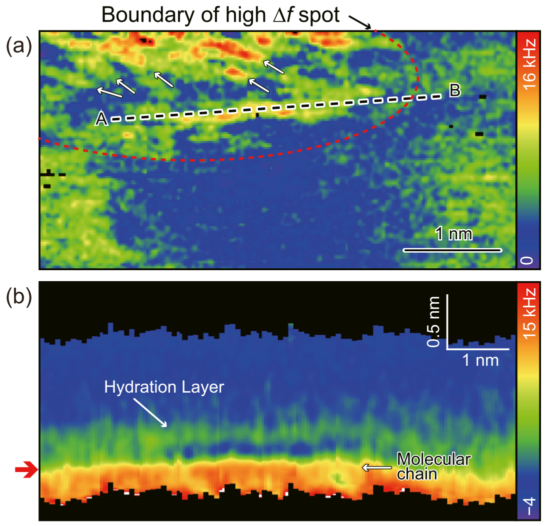

Figure 6. 3D-SFM measurements of a high Δf spot at the PVA−water interface in aq NH_3. (a) *xy* cross-section. (b) AB-z cross-section.

During the tip approach, the force exerted on a surface protrusion will exclude some of the interfacial water, leading to a compression of the protrusion. If the speed of the tip retraction is faster than the time required for the polymer chains to recover the original conformation and hydration state, a hysteresis appears in the Δf curves as shown in Figure 5(i). Thus, the E_d distribution observed in Figure 5(ii) represents the local distribution of the hydrated and swollen PVA chains. As water absorbability is one of the most important functions of a polymeric material, there have been strong demands for visualizing a nanoscale distribution of polymer absorbability. The E_d mapping method proposed here can be a powerful tool for satisfying such requirements.

The significant increase of E_d caused by ammonia (Figure 5a(ii)) suggests that it enhances hydration and swelling of PVA chains. This explains the inhibitory effect of ammonia on the silica adhesion to the PVA surface observed in the F_{ad} measurements. An adhesion of silica to a PVA surface requires the elimination of water associated with the surfaces. If ammonia can enhance the affinity of water to the PVA surface, water removal could require a larger F_l and a longer t_d. In addition, if the swollen polymer chains have high flexibility, the force exerted by a tip may only induce an elastic deformation of hydrated polymer chains.

Contact Angle (CA) Measurements. The AFM measurements suggest that ammonia enhances hydration of a PVA surface. To confirm this effect, we have performed contact angle (CA) measurements on a PVA surface with various solutions (Figure 7a). In these measurements, we used the PVA thin film instead of the PVA brush sample. If we drop water on a PVA brush, it will be quickly absorbed not only by the swelling of the PVA but also by the infiltration into the pores. Thus, it is impossible to investigate the properties of the PVA−water interface. In contrast, the PVA thin film is uniform

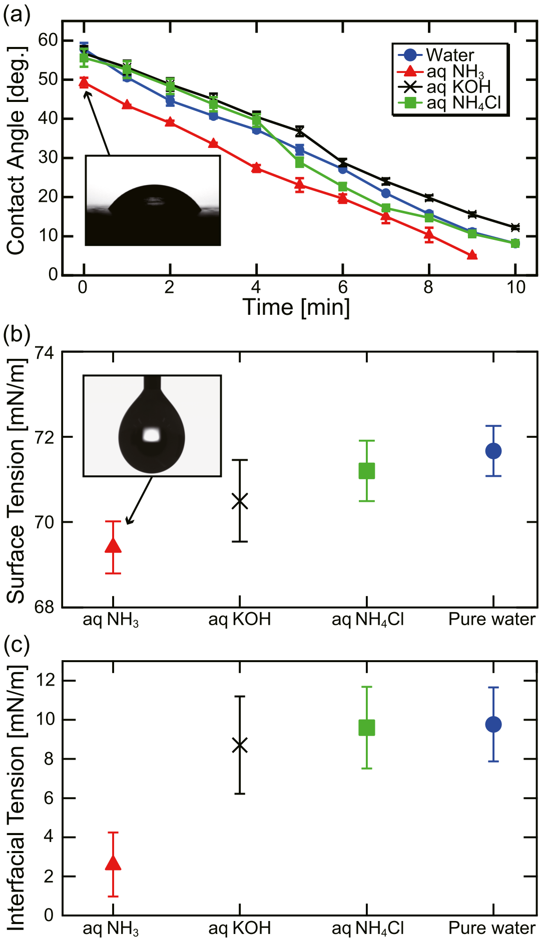

Figure 7. CA measurements on a PVA thin film formed on a HOPG substrate. The measurements were performed with pure water and aqueous solutions of NH_3, KOH, and NH_4Cl. (a) Time dependence of the CA. (b) Surface tension of individual solutions. (c) Interfacial tension of PVA−liquid interfaces.

and does not have pores. Thus, the measured CA reflects the properties at the PVA−water interface.

The CAs measured on a PVA thin film surface decreases with time (Figure 7a). This is a typical behavior for a water-soluble polymer surface. In such a case, the static CAs measured just after the water deposition could be used instead of the dynamic CAs.[46,47] Thus, the initial static CAs are plotted in Figure 7a and used for the following analysis.

To quantitatively estimate the interfacial tension, we used the Wu method, which is known to be effective for a polymer surface, and Young's equation (see Figure S4 and Tables S1 and S2 in the Supporting Information for more details). For this analysis, we measured surface tensions of individual solutions by the pendant drop method (Figure 7b) and CA of formamide on a PVA surface. The estimated interfacial tensions at the PVA−liquid interfaces are shown in Figure 7c. The result shows that pure water and aq NH_4Cl provide a similar value (∼10 mN/m) and aq KOH provides a slightly smaller value (∼8 mN/m) than that. Compared with these values, aq NH_3 provides much smaller interfacial tension (∼2.6 mN/m). This result supports our expectation that ammonia can enhance the affinity of water to a PVA surface.

MD Simulation. For the molecular-scale understanding of the role of ammonia in the hydration enhancement of a PVA surface, we have performed atomistic MD simulations of PVA−water interfaces with and without ammonia, as shown in Figure 8. As the adhesion behavior of nanoparticles to the PVA brush surface could be largely determined by the nanoscale properties of the PVA−water interfaces, molecular-scale understanding obtained by the simulation could provide important insights into the adhesion mechanism.

The simulated system consists of an equilibrated PVA slab placed at the center of a simulation box with either water or aq NH_3 filling up the regions above and below the polymer slab (Figure 8a). The slab is periodic along x- and y-axes (parallel to its surface) and in the z-axis. The simulation box length is large enough to avoid interactions between the system replicas.

After an initial equilibration of both systems, we performed 60 ns of data collection, which we used to calculate 3D densities of water, ammonia, and PVA. The full equilibration of the system PVA/water/NH_3 is expected to occur at longer time scales (of hundreds of nanoseconds) due to continuous infiltration of water. However, our intention here is to investigate the interactions between water, NH_3, and PVA at the very interface. Thus, we focused on the first 60 ns of the process.

As the upper and lower interfaces show similar behaviors (see Figure S6 for comparison), here, we only analyze density distributions near the lower interface, as shown in Figure 8. In Figure 8b−e, the time-averaged density distributions of NH_3, H_2O, and PVA are shown with green, blue, and yellow color scales, respectively. A density-dependent transparency filter was applied to each color map to make the low-density bulk region invisible (see the Supporting Information for more details). Due to this filtering and time averaging, only high-density spots with a relatively long lifetime are visualized in these density maps.

For both solutions, a mesh-like distribution of water is visualized, suggesting the formation of a hydrogen-bonding network (HBN). With an averaging of over 60 ns (Figure 8b,c), the HBNs appear to be more densely formed in pure water than in aq NH_3. However, this difference becomes less evident with an averaging of over 10 ns (Figure 8d,e). With a shorter averaging time, interfacial water and ammonia with a higher mobility are additionally visualized. Thus, the results suggest that interfacial water and ammonia in aq NH_3 are more mobile than interfacial water in pure water. This implies that interfacial ammonia enhances dynamic rearrangements of HBNs. Indeed, when we calculated the hydrogen bond lifetimes of interfacial water, we obtained an average of 41.9 ps for the aq NH_3 and 45.5 ps for the pure water system (see the Supporting Information).

Figure 8f shows xy-averaged density profiles of water, PVA, and NH_3 along the z-direction in pure water and aq NH_3. The water density profiles show almost the same profiles in both solutions, except for a slight decrease in the bulk region due to the contribution of NH_3. This result suggests that ammonia does not change the total amount of water accumulated in the interface but only enhances the dynamic rearrangements of HBNs.

As can be seen in Figure S7, although the number of H-bonds between water and PVA continuously increases in both systems due to liquid infiltration, the number of H-bonds is always lower in the aq NH_3 than that in pure water at a given time, even at longer times than 60 ns. We counted the number of hydrogen bonds (HBs) formed during 1 ns (from 59 to 60 ns) and found that 1577 water−PVA HBs are formed in pure

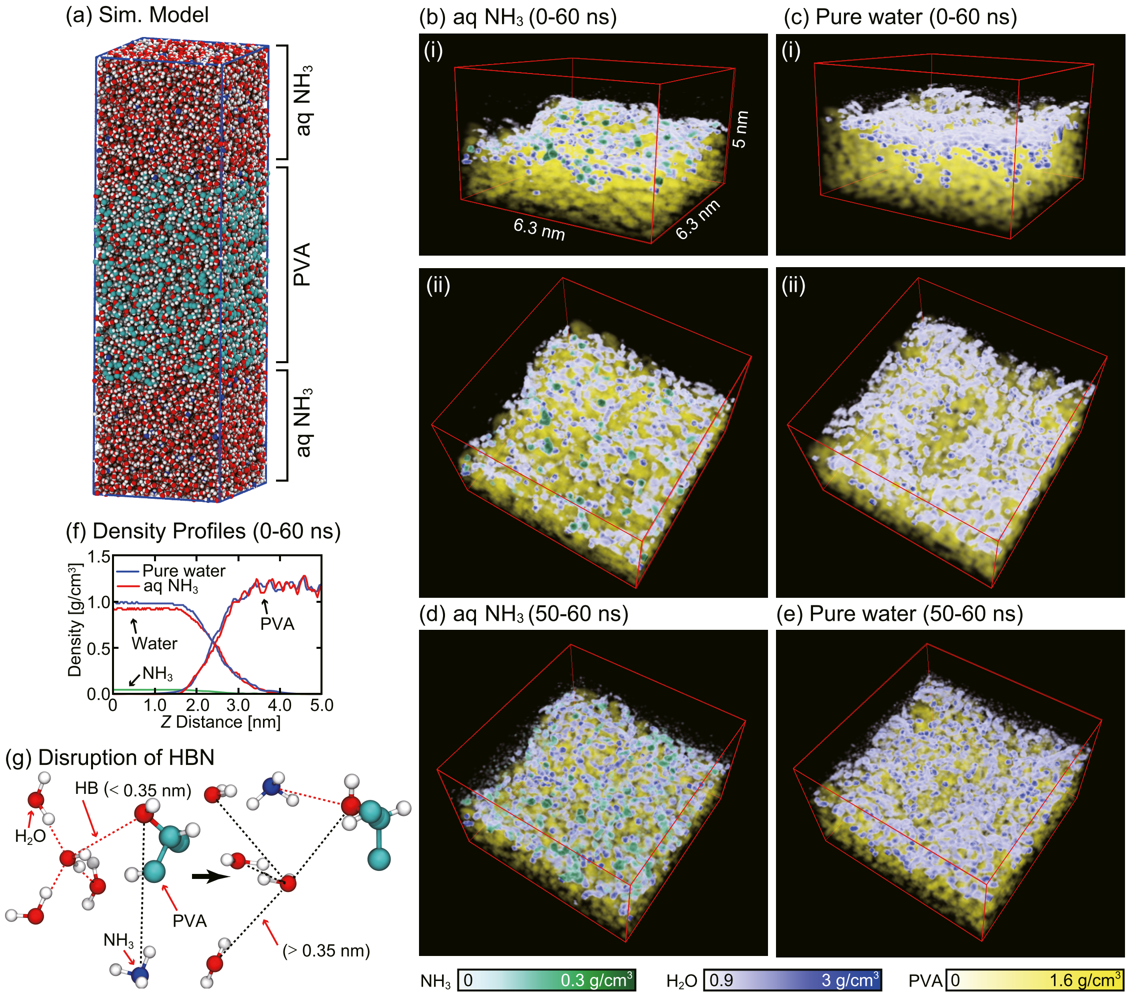

Figure 8. MD simulation of PVA–water interfaces in aq NH_3 and pure water. (a) Snapshot of the simulation model. (b–e) 3D density maps of water, ammonia, and PVA at the lower interface in (a). The densities were averaged over 0 to 60 ns for (b, c) and 50 to 60 ns for (d, e). (i, ii) in (b, c) show the same data in two different projection angles. The transparency of the rendered points was adjusted as a function of the density so that only the high-density distributions are visible. (f) *xy*-averaged density profiles of water, ammonia, and PVA derived from (b) and (c). (g) Snapshots of the simulation model before and after the disruption of the HBN caused by NH_3. The time between the frames is 26 ps. The dotted lines are drawn between the same molecules. The black lines are longer than 0.35 nm, while the red lines are shorter than 0.35 nm (i.e., hydrogen bonds).

water while 1344 water–PVA and 55 NH_3–PVA HBs are formed in aq NH_3. Even if the contribution of NH_3 is taken into account, less HBs are formed in aq NH_3 than in pure water. As the total amount of interfacial water is the same in both solutions (Figure 8f), this result suggests that NH_3 reduces interfacial water strongly bound to PVA but increases loosely bound interfacial water.

This is because NH_3 is a good hydrogen acceptor but not a good donor.[48] For example, in the snapshots shown in Figure 8g, NH_3 breaks water–water H-bonds at the PVA–liquid interface. The nitrogen atom of the NH_3 forms a HB with PVA oxygen and consequently disperses the water molecules surrounding the region. As NH_3 is a good hydrogen acceptor, it is integrated into a HBN at the interface. In fact, high-density NH_3 spots in Figure 8b,d are mostly located along HBNs. However, upon integration of NH_3, HBNs are disrupted as it is not a good hydrogen donor.

The 10 ns averaged density map (Figure 8d) shows much more high-density NH_3 spots than the 60 ns averaged one (Figure 8b). In addition, their locations are very different. These results show that NH_3 adsorption sites dynamically change their positions, which is also confirmed by a faster lateral diffusion than the water molecules (Table S3 in the Supporting Information). This NH_3 movement could cause rearrangements of HBNs, giving extra flexibility to HBNs and hence PVA chains. This flexibility could also facilitate local swelling of PVA chains, which accounts for the inhibitory effect of NH_3 against silica adhesion to a PVA surface. The model also suggests that the reduction of interfacial tension (i.e., enhanced hydration) observed by the CA measurements mainly reflects an increase of entropy caused by the enhanced mobility of water and PVA.

The HBN formed in aq NH_3 seems more uniform than that in pure water. In Figure 8c(ii), the central region shows little water distribution, while the surrounding region is covered with a high-density HBN. Thus, only PVA chains at the center may be flexible enough to swell. In contrast, in Figure 8b(ii), a low-density HBN is uniformly formed. Owing to the dynamic nature of the HBN, swelling may happen all over the interface. This is consistent with the 3D-SFM observations, where the uniform distribution of high E_d spots is observed only in aq NH_3 and they are nonuniformly distributed in other solutions (Figure 5(ii)).

https://dx.doi.org/10.1021/acsanm.0c02308

The arguments here are consistent with recent studies on the antifouling mechanism of polymer surfaces.[49−52] In these studies, water at a polymer−water interface is classified into three categories: nonfreezing water, intermediate water, and free water. Nonfreezing water is tightly bound to a surface and is noncrystallizable even at −100 °C. Intermediate water is loosely bound to a surface and crystallizes below 0 °C. Free water is scarcely bound to a surface and crystalizes at 0 °C. Among them, intermediate water is considered to play a key role in the antifouling mechanism of a polymer surface. In these studies, it was also suggested that such intermediate water enhances the flexibility of polymer chains. These previous studies, together with our present study, suggest that ammonia increases intermediate water at a PVA−water interface and thereby inhibits silica adsorption to a PVA surface.

CONCLUSIONS

In this study, we have investigated the ammonia-mediated hydration of a PVA surface and its influence on inhibition of silica nanoparticle adhesion for efficient applications of these materials to the post-CMP cleaning. The F_{ad} measurements revealed that aq NH_3 has a significant inhibitory effect on the silica nanoprobe adhesion to a PVA surface (Figure 2). Although such an effect has been expected from the negative ζ-potentials of silica nanoparticles and PVA surfaces (Figure 3), it was not directly confirmed so far. Here, we have confirmed this effect by direct measurements of F_{ad} acting between the silica nanoprobe and the PVA sample derived from the actual PVA brush for post-CMP cleaning.

Importantly, we found that this effect cannot be explained only by electrostatic interactions. The F_{ad} measured in KOH and NH_4Cl solutions is much lower than that in aq NH_3. Thus, the effect does not mainly originate from OH^- or NH_4^+, but from NH_3 molecules. In addition, the strong dependence of F_{ad} on t_d of the order of seconds suggests a significant contribution of a slow process such as dehydration and conformational changes of polymer chains. Therefore, the observed adhesion resistance could mainly originate from the hydration and steric repulsion of the polymer chains.

The 3D-SFM and CA measurements consistently support ammonia-mediated hydration and swelling of a PVA surface. The 3D-SFM measurements reveal that high E_d spots, indicating a high water absorbability, are more densely formed in aq NH_3 than in the other solutions. In addition, the molecular-scale 3D-SFM image shows that such high E_d spots consist of hydrated polymer chains. The CA measurements show that the interfacial tension in aq NH_3 is much lower than that in the other solutions, which also supports the ammonia-mediated hydration.

The MD simulations confirmed that NH_3 molecules serve as a component to form HBNs at a PVA−water interface. In addition, the simulation revealed that HBNs dynamically change their arrangements due to rapid exchanges of NH_3 adsorption sites. Such flexibility of the HBNs could facilitate local swelling of polymer chains, leading to the inhibitory effect against silica adhesion to a PVA surface.

So far, dilute ammonia water has been widely used for post-CMP cleaning, mainly for controlling the interaction between abrasive nanoparticles and a Si wafer. However, the present study demonstrates that ammonia plays a critical role in the inhibition of the nanoparticle adhesion to the PVA brush. In particular, the major contributions from the ammonia-assisted hydration and swelling of PVA chains have been totally unexpected and, hence, this finding could have great impacts on the future improvements of cleaning solutions and brush and nanoparticle materials for post-CMP cleaning.

METHODS

Samples and Solutions. For the AFM F_{ad} measurements, we used a sample derived from a PVA brush fabricated for post-CMP cleaning (Figure 1a,b). The brush material has a molecular weight of 13 200−88 000 and a degree of deacetylation over 97%. The 3D-SFM and CA measurements were performed with a PVA thin film formed on a HOPG substrate (NYD-SS, NT-MDT). Then, 30 mg of PVA powder (341 584, Merck) with 89 000−98 000 molecular weight and a degree of deacetylation over 99% was dissolved in a 30 mL of Milli-Q water by mixing at 300 rpm and 90 °C with a hot-plate magnetic stirrer, and 10 mL of the PVA solution was deposited onto a cleaved HOPG surface. A PVA thin film was formed by the spin coating at 200 rpm for 10 s and 2000 rpm for 30 s. After coating, the sample was annealed at 150 °C for 1 h in a vacuum oven.

The aqueous solutions of NH_3, KOH, and NH_4Cl used for the AFM and CA measurements were prepared as follows. Aqueous NH_3 (0.5 wt %) was prepared by mixing 0.2 mL of 28 wt % aq NH_3 (02512-95, Nacalai Tesque) and 11 mL of Milli-Q water. This solution contains 294 mM NH_3, 2.3 mM NH_4^+, and 2.3 mM OH^- (pH ≈ 11.4). Thus, most of the ammonia exists as NH_3 rather than NH_4^+ or OH^- due to its relatively low ionization constant (1.8×10^{-5} M). Aqueous KOH (2.3 mM) was prepared by dissolving the pellets of KOH (28616-45, Nacalai Tesque) into Milli-Q water to a pH of 11.4. Then, 2.3 mM aq NH_4Cl was prepared by dissolving 12.3 mg of NH_4Cl powder (02424-55, Nacalai Tesque) into 100 mL of Milli-Q water. These solutions contain either OH^- or NH_4^+ ions with the same concentration as the 0.5 wt % aq NH_3. Formamide (16229-82, Nacalai Tesque) was used for the CA measurement as purchased.

AFM Measurements. The AFM measurements were performed by a custom-built AFM with an ultralow-noise cantilever deflection sensor[53,54] and a highly stable photothermal cantilever excitation system.[55,56] The AFM was controlled by a commercially available controller (ARC2, Oxford Instruments) with a modification in the software.

For the F_{ad} measurements, we used a Si cantilever (240AC, OPUS) with a nominal spring constant (k) of 2 N/m. The tip was coated with a Si thin film by a sputter coater (KST-CSPS-KF1, K's Tech) to obtain an apex diameter of ~50 nm (Figure 1d). After immersion into water, the surface is fully oxidized so that the tip apex can mimic the structure and surface properties of a silica abrasive particle. In the F_{ad} measurements, static-mode force curves (Figure 1f) were measured with a tip velocity of 1 μm/s at 16 × 16 *xy*-arrayed positions over an area of 2 × 2 μm^2. For details of the post-processing of the obtained curves and the determination of the F_{ad} values, see Figure S2 in the Supporting Information.

For the 3D-SFM measurements, we used a Si cantilever (AC55, Olympus) with a typical k and f_0 in water of 85 N/m and 1.6 MHz, respectively. A commercially available phase-locked loop (PLL) circuit (OC4, SPECS) was used for oscillating a cantilever at its f_0 with a constant amplitude (A) and for detecting Δf induced by the force variation. In the 3D-SFM measurements, the tip was vertically scanned with a fast sinusoidal wave, while the tip was slowly scanned in the lateral direction. During the tip scan, Δf induced by the force variation was recorded to produce a 3D Δf image, with the tip−sample distance continuously regulated such that the average Δf equals to a setpoint value (Δf_{sp}). Thus, we obtain a 2D height image simultaneously with a 3D Δf image.

The pixel size of the 3D Δf images shown in Figures 4−6 are 128 × 64 × 256 pixels. The frequency of the z modulation and the lateral scan speed during the 3D-SFM imaging were 195.3 Hz and 152.59 nm/s, respectively. The individual 3D Δf images were obtained in 105 s.

The conversion from the obtained 3D Δf images to an E_d map was performed as follows. The approach and retraction curves constituting a 3D Δf image were converted to force curves using Sader's equation.[57] By integrating the force curves with respect to the z-distance, we calculated E_d for each xy position to construct a 2D E_d image.

Other Measurement Techniques. ζ-Potentials were measured with Zetasizer Nano ZS (Malvern). For the PVA surface, the PVA brush sample was prepared as described above and glued to a sample holder for the measurement system. Then, 500 nm polystyrene particles (PS500NM, MagSphere) were used as tracer particles. For the silica surface, we used 50 nm silica particles (43-00-501, Micromod). The solutions used for the measurements were prepared by adjusting the pH of Milli-Q water. HCl solution (37344-25, Nacalai Tesque) was added to reduce the pH, while NH_3 or KOH solution was added to increase the pH. The NH_3 and KOH solutions were prepared as described above.

The CA measurements were performed by DM-301 (Kyowa Interface Science) based on the half-angle method. In the measurements, 10 μL of solution was deposited on the sample surface. CA was measured every 1 min for 10 min as a function of the time lapse since the droplet was formed on the surface. We repeated this set of measurements three times. In Figure 7a, we plotted the averaged values with error bars corresponding to the standard deviations.

The interfacial tensions were measured by the same instruments based on the pendant drop method. In the measurements, a droplet was formed at the end of a stainless tube (Model No. 510, Kyowa Interface Science) with inner and outer diameters of 0.47 mm and 0.80 mm, respectively. The droplet volume was adjusted to take its maximum size just before coming off from the needle end. We performed ten measurements for each liquid. The average values are indicated in Figure 7b with error bars corresponding to the standard deviations.

MD Simulation. The molecular dynamics simulations were performed with GROMACS 2019.[58] We used the OPLS/AA force field[59] to describe the interactions of PVA and ammonia molecules. For water molecules, we used the SPC/e model.[60] For PVA, we used the partial charges calculated[61] with the Merz–Singh–Kollman method,[62,63] since they improve the solvation energies of PVA in water.

The polymer slab used in the simulations was built by randomly placing 10 PVA chains into a simulation box of size 5 × 5 × 5 nm^3. Each polymer chain consists of 50 static monomers in a head-to-tail configuration with both chains terminating in methyl groups. In this system, we initially performed an energy minimization with the conjugated gradient method[64,65] to remove close contacts between atoms that were placed too close to each other. Next, we ran 0.5 ns of molecular dynamics on the canonical ensemble (NVT, constant number of atoms, volume, and temperature) at 800 K. This high temperature is used to promote increased mobility and blending of the polymeric chains. After this step, we switched to an isothermal-isobaric ensemble (NPT, constant number of atoms, pressure, and temperature), keeping the system at 800 K but moving it toward a pressure of 1 bar and running it for 0.5 ps longer. Keeping the NPT ensemble, we then decreased the temperature to 300 K and ran dynamics for 1.25 ns. Subsequently, we switched back to the NVT ensemble and ran the system for an additional 0.5 ns.

This procedure results in a bulk PVA simulation box of 3.12705 × 3.12705 × 3.12705 nm^3. After this, we replicated this system 2 × 2 × 3 times in the x-, y-, and z-directions and repeated the same procedure used in the smaller system. However, we ran the second NPT simulation for 2 ns instead of 1.25 ns. This resulted in a bulk PVA box of 6.30231 × 6.30231 × 9.45347 nm^3 and a total of 120 polymeric chains and a density of 1.19 g/cm^3, comparable to the experimental density of bulk PVA. Next, to make the PVA slab, we removed the periodicity in the z-axis of this bulk PVA and increased the box length on that axis to 30 nm. Due to the periodicity removal, the slab surface needed further equilibration; therefore, we ran a final batch of simulations. We performed an energy minimization followed by molecular dynamics at 800 K for 3 ns and at 300 K for 6 ns, both on the NVT ensemble.

We used this equilibrated slab as the initial PVA structure in both water and aq NH_3. For the water system, we filled the empty space of the PVA slab box with 15 000 water molecules. In the aq NH_3 system, we put 14 250 water and 750 ammonia molecules. This results in a concentration of 5%, which is 10 times higher than that in the experiments. We performed simulations with 0.5, 1, and 5% concentrations and chose to display the highest concentration because the larger number of NH_3 molecules would be better sampled in the trajectory time (60 ns) used for the construction of the density maps. The dynamical properties, such as lateral diffusion coefficients (Table S3), are not significantly affected by these different concentrations.

The system configuration is such that there are 2 PVA–liquid interfaces, and Figure 8a shows the PVA at the center and aq NH_3 slabs (5 nm thick each) covering both PVA sides. However, these aq NH_3 slabs are themselves periodic as the top of the simulation box is connected to the bottom of its replica. Due to this, there are no water–vacuum interfaces in our configuration. The total thickness of the aq NH_3 (10 nm) is sufficiently large to obtain bulk density at distances far away from the PVA–liquid interface and avoid interactions between PVA–PVA slab replicas.

In both systems, we performed an energy minimization, followed by 2 ns of dynamics at 300 K on the NVT ensemble. Next, we switched to the NPT ensemble, where we ran the system for 5 ns and allowed only the box length in the z-axis to move to achieve the right densities for the liquids in our systems. Finally, we switched back to the NVT ensemble, running the systems for 62 ns each. For data acquisition, we discarded the first 2 ns of this last trajectory, obtaining 60 ns of equilibrated structures for analysis.

To control the temperature and pressure, we used Nosé–Hoover thermostats,[66,67] with a time constant of 0.2 ps, and Parrinello–Rahman barostats,[68,69] with a time constant of 2 ps. For Lennard-Jones and electrostatic interactions, a cutoff of 10 Å was used, calculating the long-range electrostatics with the particle mesh Ewald method.[70]

The 3D densities were calculated by dividing the simulation box into voxels with a bin size of 0.25 Å and averaging the atom counts in chunks of 10 ns as well the full trajectory (60 ns). For the HB analysis, we considered a distance cutoff of 3.5 Å between the donor–acceptor and a hydrogen donor–acceptor angle cutoff of 30°.

■ ASSOCIATED CONTENT

Supporting Information

The Supporting Information is available free of charge at https://pubs.acs.org/doi/10.1021/acsanm.0c02308.

> TEM images of the Si-coated AFM probes observed before and after the adhesion force measurements (Figure S1); data processing methods used for the force mapping data (Figure S2); comparison between 3D-SFM images measured on the PVA brush and PVA thin film samples (Figure S3); methods used for estimating interfacial tensions from the CA measurement results (Figure S4); visualization method for the simulated 3D density maps shown in Figure 8 (Figure S5); comparison between the simulated 3D density maps at the upper and lower interfaces (Figure S6); additional simulation analysis of HBs and diffusion coefficients of water and NH_3 (Figure S7); CA values measured with various liquids and interfacial and surface tensions estimated from them (Table S1); surface tensions, and their dispersive and polar parts for water, formamide, and PVA (Table S2); and lateral diffusion coefficients of water and NH_3 (Table S3) (PDF)

■ AUTHOR INFORMATION

Corresponding Authors

Ygor Morais Jaques − *Department of Applied Physics, Aalto University, FI-00076 Helsinki, Finland;* orcid.org/0000-0003-0114-9854; Email: ymjaques@gmail.com

Takeshi Fukuma − *Division of Electrical Engineering and Computer Science, Kanazawa University, 920-1192 Kanazawa, Japan; Nano Life Science Institute (WPI-NanoLSI) and Faculty of Frontier Engineering, Kanazawa University, 920-1192 Kanazawa, Japan;* orcid.org/0000-0001-8971-6002; Email: fukuma@staff.kanazawa-u.ac.jp

Authors

Takahiko Ikarashi − *Division of Electrical Engineering and Computer Science, Kanazawa University, 920-1192 Kanazawa, Japan;* orcid.org/0000-0001-7794-9773

Takumi Yoshino − *Division of Electrical Engineering and Computer Science, Kanazawa University, 920-1192 Kanazawa, Japan*

Naoki Nakajima − *Division of Electrical Engineering and Computer Science, Kanazawa University, 920-1192 Kanazawa, Japan*

Kazuki Miyata − *Division of Electrical Engineering and Computer Science, Kanazawa University, 920-1192 Kanazawa, Japan; Nano Life Science Institute (WPI-NanoLSI) and Faculty of Frontier Engineering, Kanazawa University, 920-1192 Kanazawa, Japan;* orcid.org/0000-0002-1641-2160

Keisuke Miyazawa − *Division of Electrical Engineering and Computer Science, Kanazawa University, 920-1192 Kanazawa, Japan; Nano Life Science Institute (WPI-NanoLSI) and Faculty of Frontier Engineering, Kanazawa University, 920-1192 Kanazawa, Japan;* orcid.org/0000-0002-5012-8040

Adam S. Foster − *Department of Applied Physics, Aalto University, FI-00076 Helsinki, Finland; Nano Life Science Institute (WPI-NanoLSI), Kanazawa University, 920-1192 Kanazawa, Japan;* orcid.org/0000-0001-5371-5905

Megumi Uno − *EBARA Corporation, 144-8510 Tokyo, Japan;* orcid.org/0000-0001-8673-0124

Chikako Takatoh − *EBARA Corporation, 144-8510 Tokyo, Japan;* orcid.org/0000-0001-5666-6037

Complete contact information is available at:
https://pubs.acs.org/10.1021/acsanm.0c02308

Notes

The authors declare no competing financial interest.

■ ACKNOWLEDGMENTS

This work was supported by the World Premier International Research Center Initiative (WPI), MEXT, Japan; JSPS KAKENHI (No. 20H00345); and the JST Mirai-Project (No. 18077272). Y.M.J. and A.S.F. were supported by the Academy of Finland (project No. 314862).

■ REFERENCES

(1) Zhang, L.; Raghavan, S.; Weling, M. Minimization of chemical-mechanical planarization (CMP) defects and post-CMP cleaning. *J. Vac. Sci. Technol., B* **1999**, *17*, 2248.

(2) Diane Hymes, J. Z.; Malik, I.; Emami; Brush, R. scrubbing emerges as future wafercleaning technology. *Solid State Technol.* **1997**, *40*, 209.

(3) Kim, H. J.; Bohra, G.; Yang, H.; Ahn, S.-G.; Qin, L.; Koli, D. Study of the cross contamination effect on post CMP in situ cleaning process. *Microelectron. Eng.* **2015**, *136*, 36−41.

(4) Kurokawa, Y.; Hirose, H.; Moriya, T.; Kimura, C. Cleaning by brush-scrubbing of chemical mechanical polished silicon surfaces using ozonized water and diluted HF. *Jpn. J. Appl. Phys.* **1999**, *38*, 5040−5043.

(5) Chen, P.-L.; Chen, J.-H.; Tsai, M.-S.; Dai, B.-T.; Yeh, C.-F. Post-Cu CMP cleaning for colloidal silica abrasive removal. *Microelectron. Eng.* **2004**, *75*, 352−360.

(6) Singh, R. K.; Wargo, C. R.; Stockbower, D. W. PVA brush design advances for Cu/low-k post-CMP cleaning apps. *Solid State Technol.* **2008**, *51*, 54.

(7) Sun, T.; Zhuang, Y.; Li, W.; Philipossian, A. Investigation of eccentric PVA brush behaviors in post-Cu CMP cleaning. *Microelectron. Eng.* **2012**, *100*, 20−24.

(8) Hong, J.; Niu, X.; Liu, Y.; He, Y.; Zhang, B.; Wang, J.; Han, L.; Yan, C.; Zhang, J. Effect of a novel chelating agent on defect removal during post-CMP cleaning. *Appl. Surf. Sci.* **2016**, *378*, 239−244.

(9) Qi, Z.; Lu, W.; Lee, W. A novel design of brush scrubbing in post-CMP cleaning. *Int. J. Mach. Tools Manuf.* **2014**, *85*, 30−35.

(10) Tseng, W.-T.; Jha, A.; Stoll, D.; Wu, C.; McCormack, T.; Yang, J. I. C. Post Cleaning for FEOL CMP with Silica and Ceria Slurries. *ECS Trans.* **2017**, *80*, 91−99.

(11) Chang, Y.-I.; Chen, J.-W.; Cheng, W.-Y.; Jang, L. The reinforcement of the physical strength of PVA sponge through the double acetalization. *Sep. Purif. Technol.* **2018**, *198*, 100−107.

(12) Yang, L.; Tan, B.; Liu, Y.; Gao, B.; Han, C. Optimization of cleaning process parameters to remove abrasive particles in post-Cu CMP cleaning. *J. Semicond.* **2018**, *39*, No. 126002.

(13) Philipossian, A.; Mustapha, L. Tribological characterization of post-CMP brush scrubbing. *Solid State Phenom.* **2003**, *92*, 275−280.

(14) Cho, H. C.; Kim, Y. M.; Lee, H. S.; Joo, S. B.; Jeong, H. D. The Effect of PVA Brush Scrubbing on Post CMP Cleaning Process for Damascene Cu Interconnection. *Solid State Phenom.* **2009**, *145-146*, 367−370.

(15) Huang, Y.; Guo, D.; Lu, X.; Luo, J. Mechanisms for nano particle removal in brush scrubber cleaning. *Appl. Surf. Sci.* **2011**, *257*, 3055−3062.

(16) Shin, W. K.; An, J. H.; Jeong, H. D. Investigation of particle adhesion force for green nanotechnology in post-CMP cleaning. *Int. J. Precis. Eng. Manuf.* **2012**, *13*, 1125−1130.

(17) Yerriboina, N. P.; Sahir, S.; Han, S.-Y.; Hand, K.-M.; Park, J.-G. The Adhesion and Removal Mechanism of Ceria Particles for STI Post-CMP Cleaning Process. *ECS Trans.* **2019**, *92*, 157.

(18) Kim, H. J. Effect of Brush Treatment and Brush Contact Sequence on Cross Contaminated Defects during CMP in-situ Cleaning. *J. Korean Soc. Tribol. Lubr. Eng.* **2015**, *31*, 239−244.

(19) Lee, J.-H.; Poddar, M. K.; Yerriboina, N. P.; Ryu, H.-Y.; Han, K.-M.; Kim, T.-G.; Hamada, S.; Wada, Y.; Hiyama, H.; Park, J.-G. Ultrasound-induced break-in method for an incoming polyvinyl acetal (PVA) brush used during post-CMP cleaning process. *Polym. Test.* **2019**, *78*, No. 105962.

(20) Lee, J.-H.; Ryu, H.-Y.; Hwang, J.-K.; Yerriboina, N. P.; Kim, T.-G.; Hamada, S.; Wada, Y.; Hiyama, H.; Park, J.-G. A Breakthrough Method for the Effective Conditioning of PVA Brush Used for Post-CMP Process. *ECS J. Solid State Sci. Technol.* **2019**, *8*, P307−P312.

(21) Lee, J.-H.; Purushothaman, M.; Han, K.-M.; Ryu, H.-Y.; Yerriboina, N. P.; Kim, T.-G.; Wada, Y.; Hamada, S.; Hiyama, H.; Park, J.-G. Study on possible root causes of contamination from an incoming PVA brush during post-CMP cleaning. *Polym. Test.* **2019**, *77*, No. 105921.

(22) Zhang, H.; Chiao, M. Anti-fouling Coatings of Poly(dimethylsiloxane) Devices for Biological and Biomedical Applications. *J. Med. Biol. Eng.* **2015**, *35*, 143−155.

(23) Molino, P. J.; Yang, D.; Penna, M.; Miyazawa, K.; Knowles, B. R.; MacLaughlin, S.; Fukuma, T.; Yarovsky, I.; Higgins, M. J. Hydration Layer Structure of Biofouling-Resistant Nanoparticles. *ACS Nano* **2018**, *12*, 11610−11624.

(24) Tamai, Y.; Tanaka, H.; Nakanishi, K. Molecular dynamics study of polymer-water interaction in hydrogels. 1. Hydrogen-bond structure. *Macromolecules* **1996**, *29*, 6750−6760.

(25) Masuda, K.; Kaji, H.; Horii, F. Solid-State 13C NMR and 1H CRAMPS Investigations of the Hydration Process and Hydrogen Bonding for Poly(vinyl alcohol) Films. *Polym. J.* **2001**, *33*, 356−363.

(26) Wu, C. Cooperative behavior of poly(vinyl alcohol) and water as revealed by molecular dynamics simulations. *Polymer* **2010**, *51*, 4452−4460.

(27) Tesei, G.; Paradossi, G.; Chiessi, E. Influence of surface concentration on poly(vinyl alcohol) behavior at the water-vacuum interface: a molecular dynamics simulation study. *J. Phys. Chem. B* **2014**, *118*, 6946−6955.

(28) McBrierty, V. J.; Martin, S. J.; Karasz, F. E. Understanding hydrated polymers: the perspective of NMR. *J. Mol. Liq.* **1999**, *80*, 179−205.

(29) Ohgi, H.; Yang, H.; Sato, T.; Horii, F. Solid-state 13C NMR investigation of the structure and hydrogen bonding for stereoregular poly(vinyl alcohol) films in the hydrated state. *Polymer* **2007**, *48*, 3850−3857.

(30) Kumar, A. C.; Mishra, A. K. 1-Naphthol as an excited state proton transfer fluorescent probe for sensing bound-water hydration of polyvinyl alcohol. *Talanta* **2007**, *71*, 2003−2006.

(31) Peng, X.-Q.; Huang, T.; Miao, S.-K.; Chen, J.; Wen, H.; Feng, Y.-J.; Hong, Y.; Wang, C.-Y.; Huang, W. Hydration of oxalic acid-ammonia complex: atmospheric implication and Rayleigh-scattering properties. *RSC Adv.* **2016**, *6*, 46582−46593.

(32) Miao, S.-K.; Jiang, S.; Peng, X.-Q.; Liu, Y.-R.; Feng, Y.-J.; Wang, Y.-B.; Zhao, F.; Huang, T.; Huang, W. Hydration of the methanesulfonate-ammonia/amine complex and its atmospheric implications. *RSC Adv.* **2018**, *8*, 3250−3263.

(33) Huang, Y. T.; Li, Y.; Guo, D.; Meng, C. Probing particle removal in brush scrubber cleaning with fluorescence technique. *Sci. China: Technol. Sci.* **2013**, *56*, 2994−3000.

(34) Terayama, Y.; Khajornrungruang, P.; Suzuki, K.; Kusatsu, K.; Hamada, S.; Wada, Y.; Hiyama, H. Real Time Nanoscale Cleaning Phenomenon Observation during PVA Brush Scrubbing by Evanescent Field. *ECS Trans.* **2019**, *92*, 191−197.

(35) Binnig, G.; Quate, C. F.; Gerber, C. Atomic Force Microscope. *Phys. Rev. Lett.* **1986**, *56*, 930.

(36) Butt, H.-J.; Cappella, B.; Kappl, M. Force measurements with the atomic force microscope: Technique, interpretation and applications. *Surf. Sci. Rep.* **2005**, *59*, 1−152.

(37) Zhang, C.; Gong, L.; Xiang, L.; Du, Y.; Hu, W.; Zeng, H.; Xu, Z. K. Deposition and Adhesion of Polydopamine on the Surfaces of Varying Wettability. *ACS Appl. Mater. Interfaces* **2017**, *9*, 30943−30950.

(38) Engström, J.; Benselfelt, T.; Wagberg, L.; D'Agosto, F.; Lansalot, M.; Carlmark, A.; Malmstrom, E. Tailoring adhesion of anionic surfaces using cationic PISA-latexes-towards tough nanocellulose materials in the wet state. *Nanoscale* **2019**, *11*, 4287−4302.

(39) Harjumäki, R.; Zhang, X.; Nugroho, R. W. N.; Farooq, M.; Lou, Y.-R.; Yliperttula, M.; Valle-Delgado, J. J.; Österberg, M. AFM Force Spectroscopy Reveals the Role of Integrins and Their Activation in Cell-Biomaterial Interactions. *ACS Appl. Bio Mater.* **2020**, *3*, 1406−1417.

(40) Fukuma, T.; Ueda, Y.; Yoshioka, S.; Asakawa, H. Atomic-Scale Distribution of Water Molecules at the Mica-Water Interface Visualized by Three-Dimensional Scanning Force Microscopy. *Phys. Rev. Lett.* **2010**, *104*, No. 016101.

(41) Fukuma, T.; Garcia, R. Atomic- and Molecular-Resolution Mapping of Solid-Liquid Interfaces by 3D Atomic Force Microscopy. *ACS Nano* **2018**, *12*, 11785−11797.

(42) Chen, S.; Li, L.; Zhao, C.; Zheng, J. Surface hydration: Principles and applications toward low-fouling/nonfouling biomaterials. *Polymer* **2010**, *51*, 5283−5293.

(43) Yiapanis, G.; Maclaughlin, S.; Evans, E. J.; Yarovsky, I. Nanoscale wetting and fouling resistance of functionalized surfaces: a computational approach. *Langmuir* **2014**, *30*, 10617−10625.

(44) Zhang, H.; Chiao, M. Anti-fouling Coatings of Poly(dimethylsiloxane) Devices for Biological and Biomedical Applications. *J. Med. Biol. Eng.* **2015**, *35*, 143−155.

(45) Penna, M.; Ley, K. J.; Belessiotis-Richards, A.; MacLaughlin, S.; Winkler, D. A.; Yarovsky, I. Hydration and Dynamics of Ligands Determine the Antifouling Capacity of Functionalized Surfaces. *J. Phys. Chem. C* **2019**, *123*, 30360−30372.

(46) Tambe, N. S.; Bhushan, B. Micro/nanotribological characterization of PDMS and PMMA used for BioMEMS/NEMS applications. *Ultramicroscopy* **2005**, *105*, 238−247.

(47) Bhushan, B. *Modern Tribology Handbook, Volume One: Principles of Tribology and Volume Two: Materials, Coatings, and Industrial Applications*; CRC Press LLC, 2001.

(48) Ekimova, M.; Quevedo, W.; Szyc, L.; Iannuzzi, M.; Wernet, P.; Odelius, M.; Nibbering, E. T. J. Aqueous Solvation of Ammonia and Ammonium: Probing Hydrogen Bond Motifs with FT-IR and Soft X-ray Spectroscopy. *J. Am. Chem. Soc.* **2017**, *139*, 12773−12783.

(49) Nakada, M.; Ishida, H.; Furushima, Y. Structural and dynamical characterisation of intermediate water interacting polyvinyl pyrrolidone. *Materialia* **2020**, *12*, No. 100743.

(50) Kuo, A.-T.; Sonoda, T.; Urata, S.; Koguchi, R.; Kobayashi, S.; Tanaka, M. Elucidating the Feature of Intermediate Water in Hydrated Poly(ω-methoxyalkyl acrylate)s by Molecular Dynamics Simulation and Differential Scanning Calorimetry Measurement. *ACS Biomater. Sci. Eng.* **2020**, *6*, 3915−3924.

(51) Tanaka, M.; Kobayashi, S.; Murakami, D.; Aratsu, F.; Kashiwazaki, A.; Hoshiba, T.; Fukushima, K. Design of Polymeric Biomaterials: The "Intermediate Water Concept ". *Bull. Chem. Soc. Jpn.* **2019**, *92*, 2043−2057.

(52) Tanaka, M.; Sato, K.; Kitakami, E.; Kobayashi, S.; Hoshiba, T.; Fukushima, K. Design of biocompatible and biodegradable polymers based on intermediate water concept. *Polym. J.* **2014**, *47*, 114−121.

(53) Fukuma, T.; Kimura, M.; Kobayashi, K.; Matsushige, K.; Yamada, H. Development of low noise cantilever deflection sensor for multienvironment frequency-modulation atomic force microscopy. *Rev. Sci. Instrum.* **2005**, *76*, No. 053704.

(54) Fukuma, T.; Jarvis, S. P. Development of liquid-environment frequency modulation atomic force microscope with low noise deflection sensor for cantilevers of various dimensions. *Rev. Sci. Instrum.* **2006**, *77*, No. 043701.

(55) Fukuma, T. Wideband low-noise optical beam deflection sensor with photothermal excitation for liquid-environment atomic force microscopy. *Rev. Sci. Instrum.* **2009**, *80*, No. 023707.

(56) Fukuma, T.; Onishi, K.; Kobayashi, N.; Matsuki, A.; Asakawa, H. Atomic-resolution imaging in liquid by frequency modulation atomic force microscopy using small cantilevers with megahertz-order resonance frequencies. *Nanotechnology* **2012**, *23*, No. 135706.

(57) Sader, J. E.; Jarvis, S. P. Accurate formulas for interaction force and energy in frequency modulation force spectroscopy. *Appl. Phys. Lett.* **2004**, *84*, 1801−1803.

(58) Abraham, M. J.; Murtola, T.; Schulz, R.; Páll, S.; Smith, J. C.; Hess, B.; Lindahl, E. GROMACS: High Performance Molecular Simulations through Multi-Level Parallelism from Laptops to Supercomputers. *SoftwareX* **2015**, *1−2*, 19−25.

(59) Jorgensen, W. L.; Maxwell, D. S.; Tirado-Rives, J. Development and Testing of the OPLS All-Atom Force Field on Conformational Energetics and Properties of Organic Liquids. *J. Am. Chem. Soc.* **1996**, *118*, 11225−11236.

(60) Berendsen, H. J. C.; Grigera, J. R.; Straatsma, T. P. The Missing Term in Effective Pair Potentials. *J. Phys. Chem. A* **1987**, *91*, 6269−6271.

(61) Noorjahan, A.; Choi, P. Effect of Partial Atomic Charges on the Calculated Free Energy of Solvation of Poly(Vinyl Alcohol) in Selected Solvents. *J. Mol. Model.* **2015**, *21*, 58.

(62) Singh, U. C.; Kollman, P. A. An Approach to Computing Electrostatic Charges for Molecules. *J. Comput. Chem.* **1984**, *5*, 129−145.

(63) Besler, B. H.; Merz, K. M.; Kollman, P. A. Atomic Charges Derived from Semiempirical Methods. *J. Comput. Chem.* **1990**, *11*, 431−439.

(64) Hestenes, M.; Stiefel, E. Methods of Conjugate Gradients for Solving Linear Systems. *J. Res. Natl. Bur. Stand.* **1952**, *49*, 409.

(65) Reid, J. K. The Use of Conjugate Gradients for Systems of Linear Equations Possessing "Property A". *SIAM J. Numer. Anal.* **1972**, *9*, 325−332.

(66) Nosé, S. A Unified Formulation of the Constant Temperature Molecular Dynamics Methods. *J. Chem. Phys.* **1984**, *81*, 511−519.

(67) Hoover, W. G. Canonical Dynamics: Equilibrium Phase-Space Distributions. *Phys. Rev. A* **1985**, *31*, 1695−1697.

(68) Parrinello, M.; Rahman, A. Polymorphic Transitions in Single Crystals: A New Molecular Dynamics Method. *J. Appl. Phys.* **1981**, *52*, 7182−7190.

(69) Nosé, S.; Klein, M. L. Constant Pressure Molecular Dynamics for Molecular Systems. *Mol. Phys.* **1983**, *50*, 1055−1076.

(70) Darden, T.; York, D.; Pedersen, L. Particle Mesh Ewald: An N Log(N) Method for Ewald Sums in Large Systems. *J. Chem. Phys.* **1993**, *98*, 10089−10092.